



Correction to the Photometric Magnitudes of the Gaia Early Data Release 3

Lin Yang¹, Haibo Yuan², Ruoyi Zhang², Zexi Niu³, Yang Huang⁴, Fuqing Duan¹, and Yi Fang²

¹ College of Artificial Intelligence, Beijing Normal University No.19, Xijiekouwai St, Haidian District, Beijing, 100875, People's Republic of China
fqduan@bnu.edu.cn

² Department of Astronomy, Beijing Normal University No.19, Xijiekouwai St, Haidian District, Beijing, 100875, People's Republic of China; yuanhb@bnu.edu.cn

³ National Astronomical Observatories, Chinese Academy of Sciences 20A Datun Road, Chaoyang District, Beijing, People's Republic of China

⁴ South-Western Institute for Astronomy Research, Yunnan University, Kunming 650500, People's Republic of China

Received 2020 December 28; revised 2021 January 11; accepted 2021 January 13; published 2021 February 17

Abstract

In this Letter, we have carried out an independent validation of the Gaia Early Data Release 3 (EDR3) photometry using approximately 10,000 Landolt standard stars from Clem & Landolt (2013). Using a machine-learning technique, the *UBVRI* magnitudes are converted into the Gaia magnitudes and colors and then compared to those in the EDR3, with the effect of metallicity incorporated. Our result confirms the significant improvements in the calibration process of the Gaia EDR3. However, modest trends up to 10 mmag with the *G* magnitude are found for all magnitudes and colors in the $10 < G < 19$ mag range, particularly for the bright and faint ends. With the aid of synthetic magnitudes computed on the CALSPEC spectra with the Gaia EDR3 passbands, absolute corrections are further obtained, paving the way for optimal usage of the Gaia EDR3 photometry in high-accuracy investigations.

Unified Astronomy Thesaurus concepts: Astronomy data analysis (1858); Fundamental parameters of stars (555); Stellar photometry (1620)

1. Introduction

The Early Data Release 3 (EDR3) of the European Space Agency (ESA)'s space mission Gaia (Gaia Collaboration et al. 2016, 2020) has delivered not only the best astrometric information but also the best photometric data for about 1.8 billion stars (Riello et al. 2020), in terms of full sky coverage, uniform calibration at mmag level, and small photometric errors for a very wide range of magnitudes. However, due to the changes of instrument configurations, magnitude-dependent systematic errors up to 10 mmag or higher have been detected in its Data Release 2 (DR2; Riello et al. 2018, Casagrande & Vandenberg 2018; Weiler 2018; Maíz Apellániz & Weiler 2018; Niu et al. 2021, re-submitted). Thanks to significant improvements in the calibration process, the magnitude term found in the Gaia DR2 photometry is greatly reduced in the EDR3. The overall trend is no larger than 1 mmag/mag except for very blue and bright sources (Riello et al. 2020).

Due to the unprecedented photometric quality, it is challenging to identify possible problems of the Gaia photometry using external catalogs. Synthetic magnitudes from well-calibrated spectral libraries, such as CALSPEC (Bohlin et al. 2014), have been used to compare the observed ones for the Gaia DR2 (Casagrande & Vandenberg 2018; Weiler 2018; Maíz Apellániz & Weiler 2018). However, the number of available spectra is limited to a few hundred, too few to identify any fine structures in the correction curves. With about 0.5 million stars selected from the Large Sky Area Multi-Object Fibre Spectroscopic Telescope (LAMOST) Data Release 5 (DR5; Luo et al. 2015), Niu et al. (2021, re-submitted) have applied the spectroscopy-based stellar color regression method (Yuan et al. 2015a) to calibrate the Gaia DR2 $G - G_{RP}$ and $G_{BP} - G_{RP}$ colors. Systematic trends with *G* magnitude are revealed for both colors in great detail at a precision of about 1 mmag. However, contributions from each of the three Gaia magnitudes cannot be decoupled.

In this Letter, we aim to perform an independent test of the Gaia EDR3 photometry by comparing it to the Landolt standard stars. The high-quality charge-coupled device

(CCD)-based *UBVRI* photometric data from Clem & Landolt (2013, hereafter CL13) is adopted for three reasons. First, it contains about 45,000 stars, about two orders of magnitude larger than the numbers of flux standards in spectral libraries. Second, it has a wide magnitude range ($10 < G < 20$) that matches well with the Gaia photometry. Last but not least, it has five filters (*UBVRI*), including the metallicity sensitive *U* filter, making it possible to include the effect of metallicity when performing transformations between different photometric systems, which is essential but ignored in the official validation of the Gaia EDR3 (Riello et al. 2020; Fabricius et al. 2020). Using a machine-learning technique, the *UBVRI* magnitudes are trained into the Gaia magnitudes and colors and then compared to those in the Gaia EDR3. Our result confirms the significant improvements in the calibration process of the Gaia EDR3. However, modest trends with the *G* magnitude are found for all magnitudes and colors. By combining the synthetic magnitudes computed on the CALSPEC (Bohlin et al. 2014, Bohlin et al. 2020) spectra with the Gaia EDR3 passbands, we further obtain absolute corrections to the Gaia EDR3 photometry, paving the way for optimal usage of the Gaia photometry.

This Letter is organized as follows. In Section 2, we introduce our data and method. The result is presented in Section 3 and discussed in Section 4. We summarize in Section 5. Note that in this Letter, the Gaia EDR3 *G* magnitudes refer to the corrected ones (phot_g_mean_mag_corrected; Riello et al. 2020).

2. Data and Method

2.1. Data

In this work, we only use main-sequence stars that have high-precision photometry from both the Gaia EDR3 and CL13. The following criteria are adopted to guarantee data quality:

- (1) $\text{err}(U) < 0.02$ mag, $\text{err}(B) < 0.015$ mag, and $\text{err}(V, R, I) < 0.01$ mag to exclude stars of poor Landolt photometry;

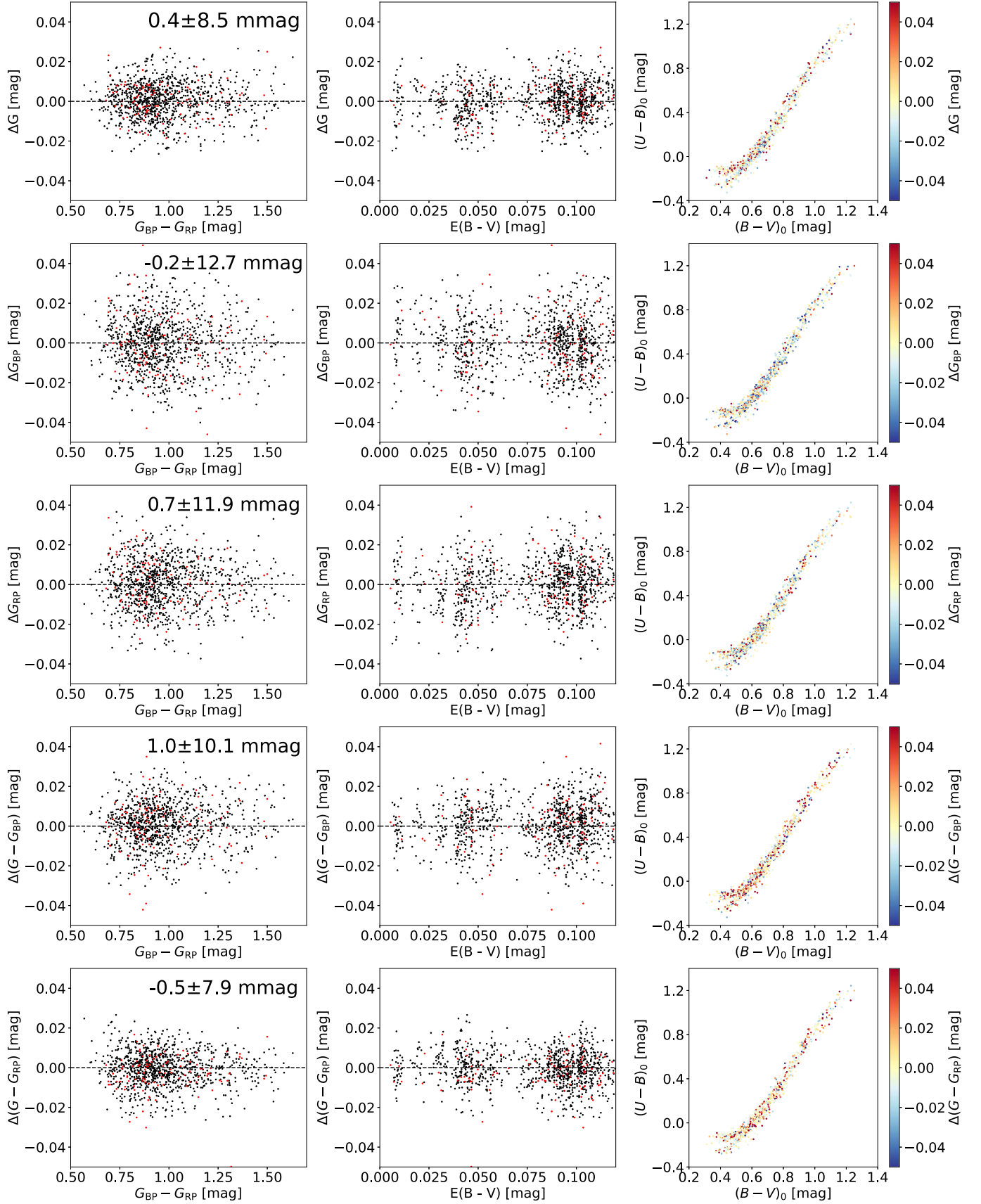


Figure 1. Residual distributions as functions of $G_{BP} - G_{RP}$ (left panel), reddening (middle panel), and in the $(U - B)_0 - (B - V)_0$ diagram (right panel) of the training (black dots) and test (red dots) samples for each of the five MLP networks. From top to bottom are the results for G , G_{BP} , G_{RP} , $G - G_{BP}$, and $G - G_{RP}$, respectively. The median values and standard deviations of the residuals are also marked in the left panels. For the reddening correction of the $U - B$ and $B - V$ colors, the SFD reddening map and reddening coefficients of 0.708 and 0.884 are adopted (Schlafly & Finkbeiner 2011).

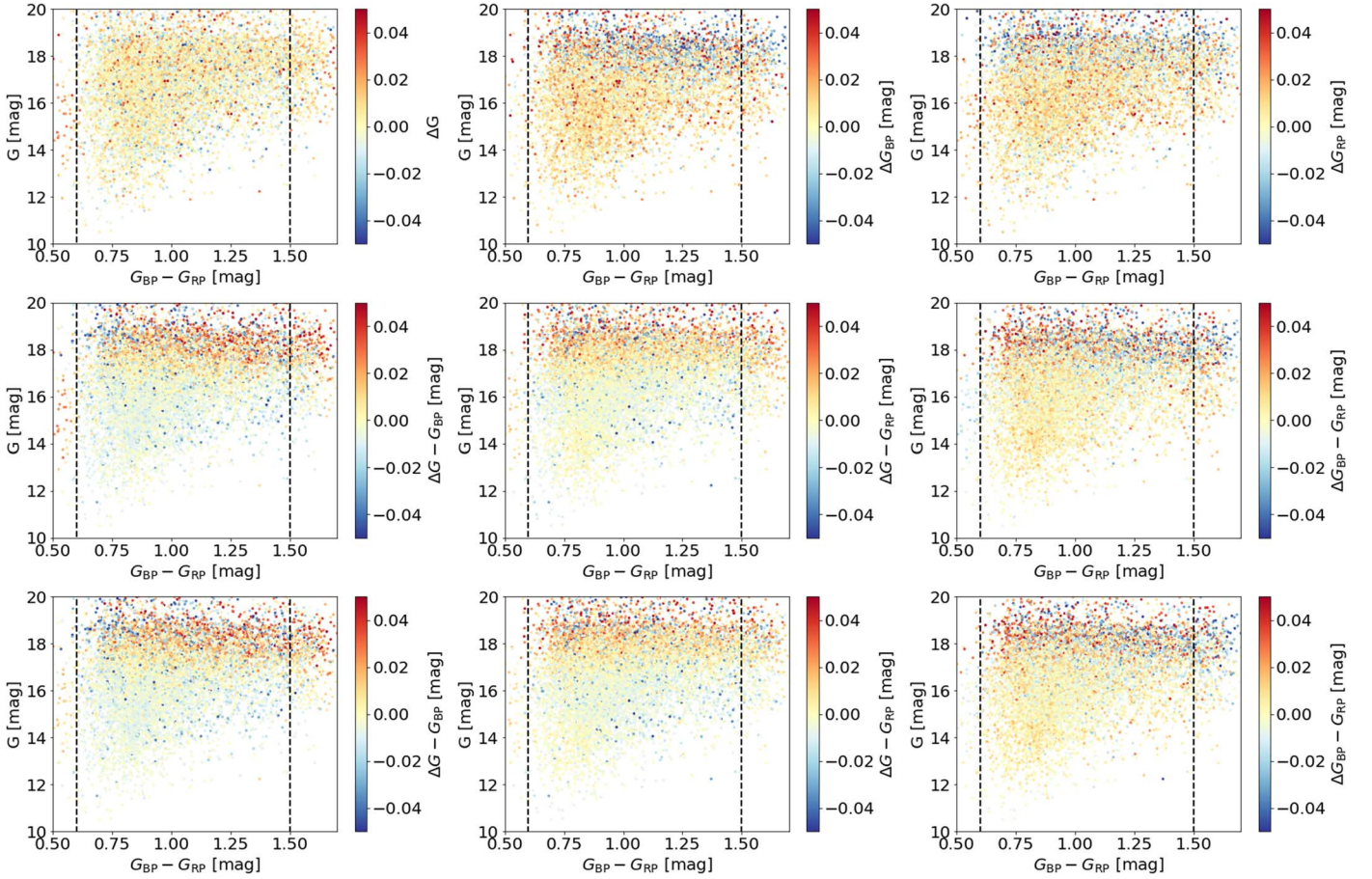


Figure 2. Residual distributions in the $(G_{BP} - G_{RP})$ — G diagram for the whole data set. The top panels show the results of the Gaia magnitudes. The middle panels show the results of the Gaia colors calculated from the top panels. The two left panels in the bottom show the results of the Gaia colors directly trained from the neural networks, while the right one the result calculated from the two left panels. The two vertical dashed lines indicate $G_{BP} - G_{RP}$ color of 0.6 and 1.5 mag, respectively.

- (2) $\text{phot_bp_rp_excess_factor} < 1.26 + 0.04 * (G_{BP} - G_{RP})^2$ to exclude stars of poor Gaia photometry (Evans et al. 2018). Note the above criterion is almost identical to requiring the corrected $\text{phot_bp_rp_excess_factor}$ (Riello et al. 2020) < 0.08 ;
- (3) $E(B - V)_{\text{SFD}} < 0.12$ mag to exclude stars of high extinction, where $E(B - V)_{\text{SFD}}$ is from the Schlegel et al. (1998, hereafter SFD) dust-reddening map;
- (4) $0.35 < B - V < 1.3$ mag to select F/G/K stars;
- (5) $G_0 > 4 * (G_{BP-RP} - 1.33 * E(B - V)_{\text{SFD}})$ to exclude giant stars, where G_0 is the intrinsic G magnitude. Here we adopt an extinction coefficient of 2.5 for the G band and a reddening coefficient of 1.33 for the $G_{BP} - G_{RP}$ color (Chen et al. 2019).

Finally, 10,294 stars are selected, including 1539 stars of $17 < G < 17.5$ mag as the reference sample. The $17 < G < 17.5$ magnitude range is adopted in order to (1) have a large number of reference stars and (2) have a relatively wide range in metallicity. For the reference sample, we further exclude a few hundred stars whose magnitude errors are larger than 0.01 mag in the U band or 0.005 mag in the $B/V/R/I$ band. The remaining 1,079 stars are divided into two groups: the training set (90%) and the test set (10 percent). For the whole sample, the median errors are 4.3, 3.3, 2.3, 1.9, and 2.3 mmag for U, B, V, R, I , and 2.8, 7.7, and 6.1 mmag for G, G_{BP}, G_{RP} , respectively. For the reference sample, the median errors are

3.6, 2.9, 1.9, 1.6, and 1.9 mmag for U, B, V, R, I , and 2.9, 9.2, and 7.1 mmag for G, G_{BP}, G_{RP} , respectively.

2.2. Method

In this work, multi-layer perceptron neural networks (MLPs) with architectures of 4-128-64-8-1 are designed to convert the Landolt $UBVRI$ photometry of CL13 into the Gaia EDR3 magnitudes and colors. Each node of the hidden layers and the output layer is connected to all nodes of its previous layer, with a nonlinear function:

$$f(X) = g(WX + b) \quad (1)$$

where W and b , respectively, represent the weight metric and bias vector, $g(\bullet)$ represents the LeakyReLU activation function with negative slope coefficient $\alpha = 0.1$ in the hidden layer. Five MLPs are trained: three for the Gaia EDR3 magnitudes and two for the Gaia EDR3 colors. The four input colors are the same for the five MLPs, i.e., $U - B, B - V, V - R, R - I$. The outputs are $G - A, G_{BP} - A, G_{RP} - A, G - G_{BP}$, and $G - G_{RP}$, respectively, where A is an artificial magnitude defined as the mean of the B, V, R magnitudes. Note that in this work, observed magnitudes/colors are preferred to dereddened ones, to avoid possible systematic errors caused by reddening correction. Systematic errors may come from at least two aspects: spatially dependent systematic errors with the SFD

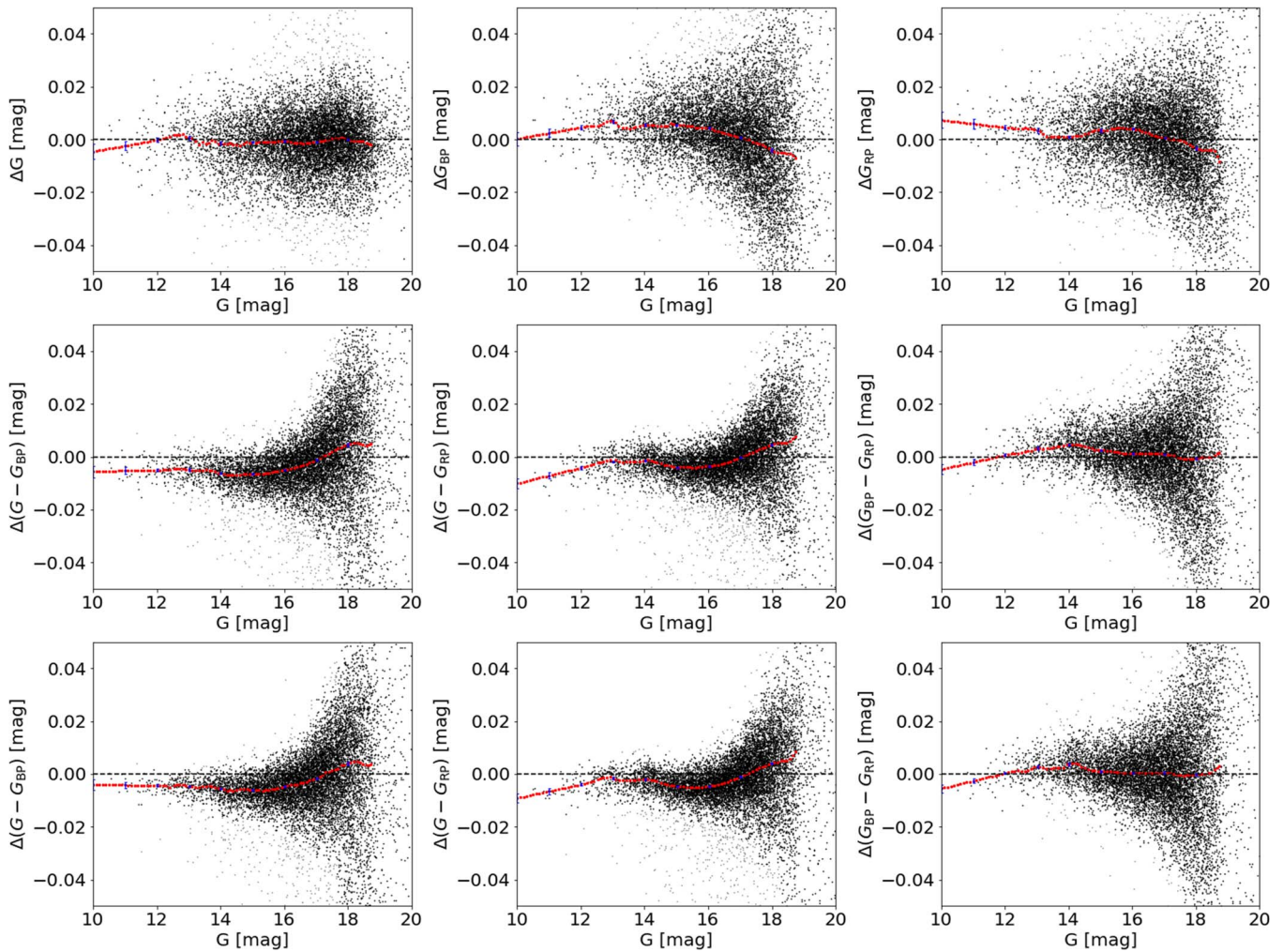


Figure 3. Residual distributions as a function of G magnitude for the whole data set after excluding stars of $G_{BP} - G_{RP} < 0.6$ and $G_{BP} - G_{RP} > 1.5$. The panels are arranged in the same way to Figure 2. For each panel, stars are divided into different bins of width of 0.4 mag at a step size of 0.1 mag when $12.5 < G < 18.7$ mag. The median value for each bin is estimated, with a $3 - \sigma$ clipping performed and the gray dots dropped. At the bright end, a linear fitting is performed for stars of $G < 13.0$ mag, the results are adopted when $G < 12.5$ mag. Finally, a locally estimated scatterplot smoothing (LOWESS) is applied to smooth the calibration curves, with $frac = 0.07$. The final results are indicated by red dotted lines. The blue error bars are estimated with 500 subsamples using the Bootstrap method.

reddening map (Sun et al., to be submitted; Niu et al. 2021) and overestimates of reddening for bright local stars.

The training process is carried out with Keras 2.2.4 and Tensorflow 1.12. The loss function, mean squared error (MSE) with a L_2 regularized term, is optimized using adaptive moment estimation (ADAM; Kingma & Ba 2014) with a mini-batch size of 900 samples. The trade-off coefficient between the MSE and regularized term is 0.000001 to avoid overfitting. Other hyper-parameters set manually in our work are training iterations $epoch = 100,000$ and learning rate $\eta = 0.00001$.

During the training process, a 3σ clipping is performed to exclude outliers. Then, the training process runs again with the same hyper-parameters. After the networks are well trained, we apply the models to the whole data set. The predicted magnitudes and colors are then obtained and compared to those in the EDR3. The median differences (predicted – observed) as a function of G magnitude are regarded as the calibration curves.

3. Result

Figure 1 shows the results of the training and test samples for different MLP neural networks. It can be seen that the residuals

show no dependence on the $G_{BP} - G_{RP}$ color or the SFD reddening. The residuals also show no systematic patterns in the $(U - B)_0 - (B - V)_0$ diagram. Because dwarf stars of different metallicities are well separated in the $(U - B)_0 - (B - V)_0$ diagram (e.g., Sandage & Smith 1963), the results suggest that the effect of metallicity has been fully taken into account in our neural networks. Note that the standard deviations of the residuals are 8.5, 12.7, 11.9, 10.1, and 7.9 mmag for the G , G_{BP} , G_{RP} , $G - G_{BP}$, and $G - G_{RP}$, respectively. The small standard deviations suggest that the Gaia photometry can be well recovered from the Landolt photometry, to a precision of about 1 percent with photometric errors included.

Figure 2 shows the residual distributions in the $(G_{BP} - G_{RP}) - G$ diagram for the whole data set. No obvious dependence on color within the two dashed lines is seen for all the panels, which is consistent with the result of Riello et al. (2020). For a few stars of $G_{BP} - G_{RP} < 0.6$ or $G_{BP} - G_{RP} > 1.5$, there exist some discrepancies, probably caused by the boundary effect in the training process. Those stars are excluded in the following analysis.

The calibration curves as a function of G magnitude for the Gaia magnitudes and colors are plotted in Figure 3. The errors are also estimated using the Bootstrap method with 500

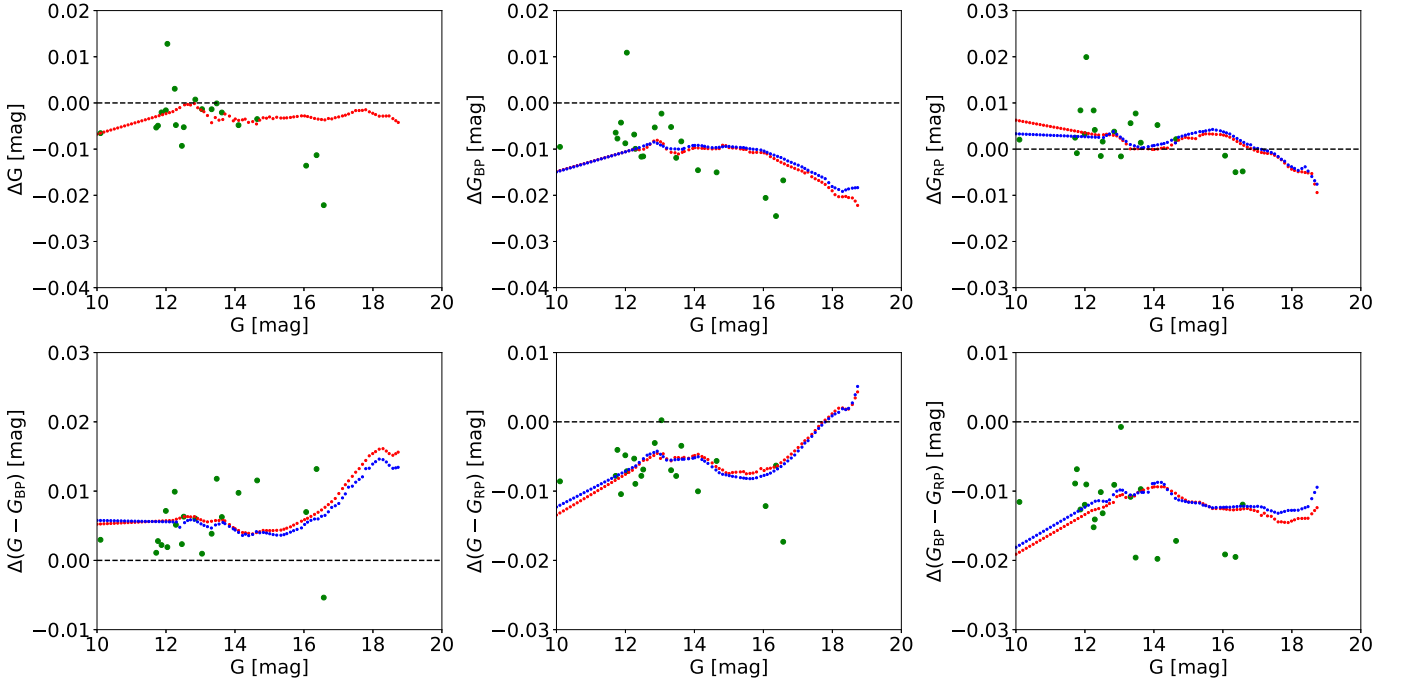


Figure 4. Magnitude (top panels) and color (bottom panels) calibration curves. The green dots are results from synthetic magnitudes/colors of the CALSPEC spectra. The red dotted lines are results from the trained magnitudes. The blue dotted lines in the two top panels on the right are results combining the trained G magnitude and trained $G - G_{BP}$ and $G - G_{RP}$ colors. The blue dotted lines in the bottom panels are results from the trained colors. All the dotted lines are shifted by the median of the differences between the dotted lines and the green dots to match the green dots.

subsamples. The errors at $G \sim 12.0, 13.0, 14.0, 16.0,$ and 18.0 mag are, respectively, (0.9, 0.8, 0.6, 0.4, 0.4), (0.7, 0.7, 0.5, 0.3, 0.7), and (0.9, 0.9, 0.3, 0.3, 0.6) mmag in the top panels from left to right, (0.6, 0.8, 0.2, 0.2, 0.6), (0.6, 0.4, 0.2, 0.2, 0.5), and (0.5, 0.5, 0.2, 0.2, 0.5) mmag in the middle panels from left to right, (0.5, 0.3, 0.2, 0.2, 0.6), (0.5, 0.6, 0.4, 0.2, 0.4), and (0.4, 0.5, 0.5, 0.3, 0.4) mmag in the bottom panels from left to right. Our result confirms the significant improvements in the calibration process of the Gaia EDR3. The strong trend in G as a function of G in DR2 is greatly reduced. However, modest trends with G magnitude are found for all magnitudes and colors. A tiny discontinuity of 2–3 mmag at $G \sim 13$ mag is clearly detected for all the magnitude curves, which is probably related to a change in the instrument configuration. The downturn at faint magnitudes visible in the G_{BP} and G_{RP} passbands is possibly caused by some over-estimation of the background in the BP and RP spectra. Therefore, the trend in $G_{BP} - G_{RP}$ as a function of G is much weaker compared to that in $G - G_{BP}$ and $G - G_{RP}$.

In the above analysis, we have assumed that the corrections are zero for stars of $17 < G < 17.5$ mag, which is not true. To set an absolute correction zero-point, synthetic magnitudes of G , G_{BP} , and G_{RP} are computed on the CALSPEC (Bohlin et al. 2014, 2020) spectra with the Gaia EDR3 passbands, with the same approach of Riello et al. (2020). The results are used to obtain the absolute corrections. Only 20 stars of $G_{BP} - G_{RP} > -0.3$, $G > 10$, and $\text{phot_bp_rp_excess_factor} < 1.26 + 0.04 * (G_{BP} - G_{RP})^2$ are used. The mean magnitude offsets are $-4.2, -9.5,$ and 3.0 mmag for $G, G_{BP},$ and G_{RP} , respectively. The shifts of the calibration curves are $-2.1, -15.1, -1.0, 9.9,$ and -3.1 mmag for $G, G_{BP}, G_{RP}, G - G_{BP},$ and $G - G_{RP}$, respectively. The final calibration curves are plotted in Figure 4 and listed in Table 1. Note that only results directly obtained from the five MLPs (red lines in the top panels

of Figure 4 and blue lines in the two bottom panels on the left) are given in Table 1. Calibration curves yielded by different MLPs (blue and red dotted lines in Figure 4) agree with each other very well, with a typical difference of 0.5 mmag, within the training errors.

4. Discussion

Fabricius et al. (2020) compared Gaia EDR3 photometry to a number of external catalogs in their Figure 34, including the one we use in the current work. They select all stars of $|b| > 30^\circ$ and $A_V < 0.05$ mag for low-latitude stars. Simple color–color relations are then used, $X = V + f(V - I)$ where X denotes Gaia magnitude, to transform the Landolt V, I magnitudes into Gaia magnitudes.

Stellar colors depend mainly on the stellar effective temperature, but also to a fair degree on metallicity, particularly the blue colors. Yuan et al. (2015b) proposed using the metallicity-dependent stellar locus to better describe the transformation relations between different colors. Taking the Sloan Digital Sky Survey (SDSS) colors, for example, at a given $g - i$ color, they find that typically 1 dex decrease in metallicity causes 0.20 and 0.02 mag decrease in colors $u - g$ and $g - r$ and 0.02 and 0.02 mag increase in colors $r - i$ and $i - z$, respectively. The variations are larger for more metal-rich stars, and for F/G/K stars. The relations are also different between dwarf stars and giant stars. Therefore, to make optimal transformations between different colors, the metallicity effect shall be taken into account. Huang et al. (2020) have applied a revised stellar color regression method to re-calibrate the SkyMapper Southern Survey DR2 (Onken et al. 2019), achieving a uniform calibration with precision better than 1% by considering the effect of metallicity on stellar colors. López-Sanjuan et al. (2021) have discussed the impact of metallicity on photometric calibration of the Javalambre Photometric Local Universe Survey (J-PLUS; Cenarro et al. 2019) with the

Table 1
Magnitude and Color Calibration Curves in Units of Mmag

G	ΔG	ΔG_{BP}	ΔG_{RP}	$\Delta(G - G_{\text{BP}})$	$\Delta(G - G_{\text{RP}})$
10.0	-6.7	-14.9	6.3	5.8	-12.3
10.4	-5.9	-14.0	5.7	5.7	-11.3
10.8	-5.0	-13.1	5.2	5.7	-10.2
11.2	-4.1	-12.3	4.6	5.7	-9.2
11.6	-3.2	-11.4	4.1	5.6	-8.2
12.0	-2.3	-10.6	3.5	5.6	-7.1
12.4	-1.0	-10.1	3.1	4.8	-5.9
12.5	-0.6	-10.0	3.1	5.3	-5.4
12.6	-0.4	-9.7	3.2	5.7	-5.0
12.7	-0.4	-9.1	3.1	5.8	-4.7
12.8	-0.2	-8.4	3.0	5.8	-4.5
12.9	-0.9	-8.1	2.9	5.6	-4.3
13.0	-1.4	-8.4	2.5	5.3	-4.6
13.1	-1.9	-8.9	1.9	5.1	-5.1
13.2	-2.7	-10.0	1.1	4.9	-5.5
13.3	-4.0	-10.6	0.2	4.7	-5.5
13.4	-3.5	-10.8	0.1	5.0	-5.5
13.5	-3.5	-11.0	0.1	5.2	-5.5
13.6	-3.6	-10.8	0.1	5.4	-5.4
13.7	-2.6	-10.5	0.1	5.3	-5.4
13.8	-2.7	-10.3	0.1	5.0	-5.3
13.9	-3.4	-10.0	0.0	4.7	-5.3
14.0	-3.5	-9.7	-0.1	4.4	-5.2
14.1	-3.7	-9.7	0.0	4.1	-5.1
14.2	-3.7	-9.8	0.2	3.7	-5.4
14.3	-3.5	-9.9	0.3	3.8	-5.7
14.4	-4.2	-9.9	0.3	3.6	-6.0
14.5	-4.1	-10.0	0.8	3.7	-6.4
14.6	-4.4	-9.9	1.3	4.1	-6.9
14.7	-3.9	-9.9	1.8	4.0	-7.3
14.8	-3.3	-9.3	2.2	4.0	-7.5
14.9	-3.3	-9.2	2.5	4.0	-7.6
15.0	-3.0	-9.7	2.4	3.9	-7.8
15.1	-3.4	-9.8	2.4	3.7	-7.9
15.2	-3.1	-9.8	2.3	3.7	-7.9
15.3	-3.2	-9.9	2.7	3.6	-8.0
15.4	-3.3	-10.0	3.1	3.7	-8.1
15.5	-3.2	-10.1	3.3	3.9	-8.2
15.6	-3.1	-10.6	3.3	4.1	-8.2
15.7	-3.0	-10.8	3.3	4.3	-8.2
15.8	-2.9	-10.7	3.2	4.5	-8.1
15.9	-2.8	-10.7	3.2	4.6	-7.9
16.0	-2.8	-10.8	3.1	5.1	-7.8
16.1	-2.9	-11.0	2.9	5.5	-7.6
16.2	-3.1	-11.6	2.6	5.8	-7.4
16.3	-3.3	-12.0	2.2	6.0	-7.1
16.4	-3.5	-12.4	1.7	6.0	-6.8
16.5	-3.6	-12.8	1.2	6.3	-6.5
16.6	-3.7	-13.2	0.8	6.5	-6.1
16.7	-3.4	-13.5	0.5	7.0	-5.7
16.8	-3.5	-13.8	0.1	7.6	-5.3
16.9	-3.2	-14.1	-0.2	7.9	-4.8
17.0	-3.0	-14.5	-0.5	8.2	-4.3
17.1	-2.8	-14.7	-0.7	8.9	-3.7
17.2	-2.7	-15.2	-0.8	9.6	-3.1
17.3	-2.4	-15.0	-0.9	10.6	-2.7
17.4	-2.1	-16.0	-1.0	10.7	-2.1
17.5	-1.7	-16.4	-1.3	11.3	-1.5
17.6	-1.6	-16.8	-1.8	11.7	-1.0
17.7	-1.6	-17.2	-2.3	12.1	-0.4
17.8	-1.5	-17.7	-3.1	13.2	0.0
17.9	-1.9	-18.4	-3.8	13.3	0.5
18.0	-2.3	-19.1	-4.4	13.9	0.9
18.1	-2.6	-20.0	-4.7	14.3	1.2
18.2	-2.9	-20.3	-4.9	14.6	1.4

Table 1
(Continued)

G	ΔG	ΔG_{BP}	ΔG_{RP}	$\Delta(G - G_{\text{BP}})$	$\Delta(G - G_{\text{RP}})$
18.3	-2.8	-20.3	-4.9	14.5	1.9
18.4	-2.8	-20.3	-5.1	14.1	1.8
18.5	-3.0	-20.5	-5.2	13.6	2.2
18.6	-3.5	-20.8	-5.9	13.3	3.0
18.7	-4.0	-21.8	-8.6	13.4	4.6

stellar locus technique and found significant improvements for blue passbands.

A large vertical metallicity gradient of the Galaxy at the solar neighborhood is widely reported, e.g., $0.15 \text{ dex kpc}^{-1}$ from Huang et al. (2015). Considering the strong correlation between stellar magnitudes and distances for dwarf stars, it implies a strong correlation between stellar magnitudes and metallicities, especially for high Galactic latitude regions. Such a correlation could cause magnitude-dependent systematic errors when adopting simple color-color relations and ignoring the effect of metallicity, at the level of from several mmag to tens of mmag for the Gaia passbands, depending on which colors are used and properties of the sample stars. In our work, by making use of the full color information of the Landolt photometry, particularly the $U-B$ color, we can naturally incorporate the effect of metallicity and obtain robust results.

To validate our result, following the procedure in Niu et al. (2021), re-submitted), we select a high-quality common sample containing 0.7 million stars in LAMOST Data Release 7 (DR7) and Gaia EDR3 and plot the residuals from the $G - G_{\text{RP}} = f(G_{\text{BP}} - G_{\text{RP}}, [\text{Fe}/\text{H}])$ relation as a function of G in Figure 5. The top panel plots the result of the published EDR3 data, which is quite similar to Figure 32 in Fabricius et al. (2020) and shows small but well-detected magnitude dependent deviations from zero. The bottom panel plots the result after the magnitude corrections in this work. Compared to the published EDR3 data, the deviations are significantly reduced to zero along with the G magnitude, especially at the bright and faint ends. The result suggests that our corrections are valid. Note that at $G \sim 13$ mag where a discontinuity happens, our corrections are not as good as for fainter magnitudes. This is because we do not have enough stars to sample the correction curves at a very high resolution in the G magnitude.

Note that due to the limited magnitude and color ranges ($10 < G < 19$, $0.6 < G_{\text{BP}} - G_{\text{RP}} < 1.5$) of our final sample, our correction curves may not be valid for stars outside the above ranges, particularly for the bright and blue ($G < 13$ and $G_{\text{BP}} - G_{\text{RP}} < -0.1$) ones (Riello et al. 2020), and thus should be used with caution. Note also that the EDR3 photometry is calibrated in the absolute flux level using a set of spectro-photometric standard stars (SPSS; Pancino et al. 2012), whose fluxes are tied to the 2013 version of CALSPEC (Riello et al. 2020). Therefore, adjusting the absolute flux scale to the current CALSPEC library will result in an inconsistency with the uncorrected photometry. To avoid discontinuities, the calibration terms at $G = 10$ are suggested for stars brighter than $G = 10$. For stars fainter than $G = 18.7$, the calibration terms at $G = 18.7$ are suggested.

In the current MLPs, reddening values of individual stars are not included. We have performed tests by including reddening values from the SFD map into the networks, and the predicted

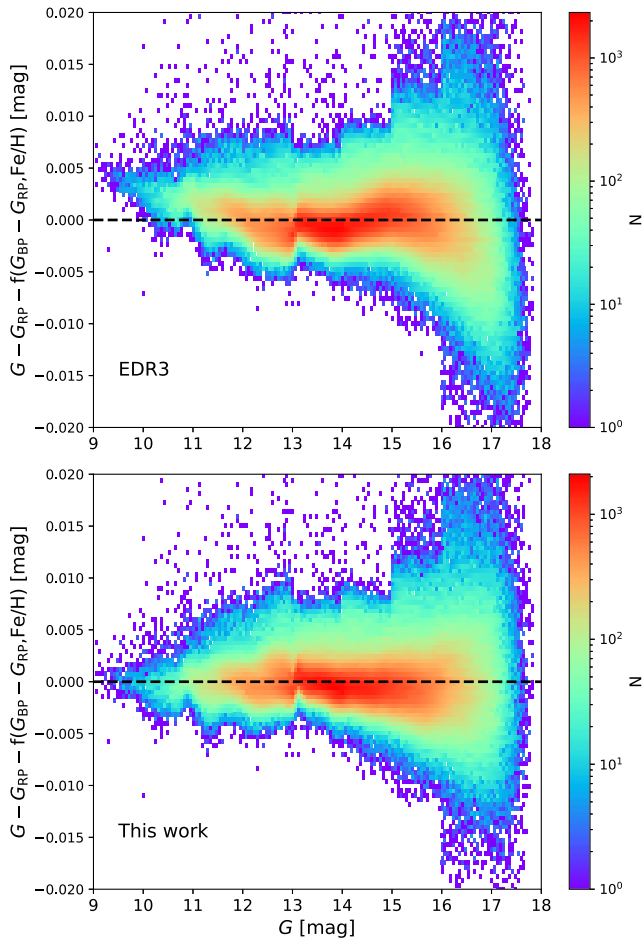


Figure 5. 2D histogram of the $G - G_{BP}$ residual after subtracting the metallicity-dependent color locus. Top panel: published EDR3 data. Bottom panel: applying magnitude corrections from this work. Note that the colors here refer to dereddened colors.

magnitudes and colors are hardly changed, suggesting that our results are insensitive to the reddening. This is not surprising because systematic errors in the reddening correction are largely canceled out.

5. Summary

In this work, we have carried out an independent validation of the Gaia EDR3 photometry using about 10,000 well-selected Landolt standard stars from Clem & Landolt (2013). Using five MLPs with architectures of 4-128-64-8-1, the $UBVRI$ magnitudes are trained into the Gaia magnitudes and colors and then compared to those in the Gaia EDR3, with the effect of metallicity fully taken into account.

Our result confirms the significant improvements in the calibration process of the Gaia EDR3. The strong trend in G as a function of G in DR2 is greatly reduced. However, modest trends with the G magnitude are found for all magnitudes and colors for the $10 < G < 19$ mag range, particularly at the bright and faint ends. A tiny discontinuity of 2–3 mmag at $G \sim 13$ mag is clearly detected for all the magnitude curves, probably related to a change in the instrument configuration. The downturn at faint magnitudes visible in the G_{BP} and G_{RP} passbands is possibly caused by some over-estimation of the background in the BP and RP spectra. The trend in $G_{BP} - G_{RP}$ as a function of G is much weaker compared to that in $G - G_{BP}$

and $G - G_{RP}$. With synthetic magnitudes computed on the CALSPEC spectra with the Gaia EDR3 passbands, absolute calibration curves are further provided (Figure 4 and Table 1), paving the way for optimal usage of the Gaia EDR3 photometry in high-accuracy investigations. In the future Gaia data releases, the effect of metallicity should be included when comparing with external catalogs.

Our result demonstrates that mapping from one set of observables directly to another set of observables with machine learning provides a promising way in the calibration and analyses of large-scale surveys.

We acknowledge the anonymous referee for valuable comments that improved the quality of this Letter. This work is supported by the National Natural Science Foundation of China through the projects NSFC 11603002, the National Key Basic R&D Program of China via 2019YFA0405503, and Beijing Normal University grant No. 310232102. Y.H. acknowledges support from the National Natural Science Foundation of China grants 11903027, 1183300, and Yunnan University grant C176220100006. This work has made use of data from the European Space Agency (ESA) mission Gaia (<https://www.cosmos.esa.int/gaia>), processed by the Gaia Data Processing and Analysis Consortium (DPAC, <https://www.cosmos.esa.int/web/gaia/dpac/consortium>). Funding for the DPAC has been provided by national institutions, in particular the institutions participating in the Gaia Multilateral Agreement. Guoshoujing Telescope (the Large Sky Area Multi-Object Fiber Spectroscopic Telescope; LAMOST) is a National Major Scientific Project built by the Chinese Academy of Sciences. Funding for the project has been provided by the National Development and Reform Commission. LAMOST is operated and managed by the National Astronomical Observatories, Chinese Academy of Sciences. This research has made use of the SIMBAD database, operated at CDS, Strasbourg, France.

ORCID iDs

Haibo Yuan <https://orcid.org/0000-0003-2471-2363>
 Ruoyi Zhang <https://orcid.org/0000-0003-1863-1268>
 Zexi Niu <https://orcid.org/0000-0002-3651-0681>
 Yang Huang <https://orcid.org/0000-0003-3250-2876>

References

- Bohlin, Ralph C. 2020, *IAUGA*, 14, 449
 Bohlin, R. C., Gordon, K. D., & Tremblay, P.-E. 2014, *PASP*, 126, 711
 Casagrande, L., & Vandenberg, D. A. 2018, *MNRAS*, 479, L102
 Cénarro, A. J., Moles, M., Cristóbal-Hornillos, D., et al. 2019, *A&A*, 622, A176
 Chen, B.-Q., Huang, Y., Yuan, H.-B., et al. 2019, *MNRAS*, 483, 4277
 Clem, J. L., & Landolt, A. U. 2013, *AJ*, 146, 88
 Evans, D. W., Riello, M., De Angeli, F., et al. 2018, *A&A*, 616, A4
 Fabricius, C., Luri, X., Arenou, F., et al. 2020, arXiv:2012.06242
 Gaia Collaboration, Brown, A. G. A., Vallenari, A., et al. 2020, arXiv:2012.01533
 Gaia Collaboration, Prusti, T., de Bruijne, J. H. J., et al. 2016, *A&A*, 595, A1
 Huang, Y., Liu, X.-W., Zhang, H.-W., et al. 2015, *RAA*, 15, 1240
 Huang, Y., Yuan, H., Li, C., et al. 2020, arXiv:2011.07172
 Kingma, D. P., & Ba, J. 2014, arXiv:1412.6980
 López-Sanjuan, C., Yuan, H.-B., Vázquez Ramírez, H., et al. 2021, arXiv:2101.12407
 Luo, A.-L., Zhao, Y.-H., Zhao, G., et al. 2015, *RAA*, 15, 1095
 Maíz Apellániz, J., & Weiler, M. 2018, *A&A*, 619, A180
 Niu, Z. X., Yuan, H.-B., & Liu, J.-F. 2021, *ApJ*, in press (arXiv:2101.04290)
 Onken, C. A., Wolf, C., Bessell, M. S., et al. 2019, *PASA*, 36, e033

Pancino, E., Altavilla, G., Marinoni, S., et al. 2012, [MNRAS](#), **426**, 1767
Riello, M., De Angeli, F., Evans, D. W., et al. 2018, [A&A](#), **616**, A3
Riello, M., De Angeli, F., Evans, D. W., et al. 2020, [arXiv:2012.01916](#)
Sandage, A., & Smith, L. L. 1963, [ApJ](#), **137**, 1057
Schlafly, E. F., & Finkbeiner, D. P. 2011, [ApJ](#), **737**, 103

Schlegel, D. J., Finkbeiner, D. P., & Davis, M. 1998, [ApJ](#), **500**, 525
Sun, Y., Yuan, H.-B., Chen, B. Q., et al. 2021, [ApJS](#), submitted
Weiler, M. 2018, [A&A](#), **617**, A138
Yuan, H.-B., Liu, X.-W., Xiang, M.-S., et al. 2015a, [ApJ](#), **799**, 133
Yuan, H.-B., Liu, X.-W., Xiang, M.-S., et al. 2015b, [ApJ](#), **799**, 134